



Chondrules reveal large-scale outward transport of inner Solar System materials in the protoplanetary disk

Curtis D. Williams^{a,1}, Matthew E. Sanborn^a, Céline Defouilloy^{b,2}, Qing-Zhu Yin^{a,1}, Noriko T. Kita^b, Denton S. Ebel^c, Akane Yamakawa^{a,3}, and Katsuyuki Yamashita^d

^aDepartment of Earth and Planetary Sciences, University of California, Davis, CA 95616; ^bWiscSIMS, Department of Geoscience, University of Wisconsin–Madison, Madison, WI 53706; ^cDepartment of Earth and Planetary Sciences, American Museum of Natural History, New York, NY 10024; and ^dGraduate School of Natural Science and Technology, Okayama University, Kita-ku, 700-8530 Okayama, Japan

Edited by H. J. Melosh, Purdue University, West Lafayette, IN, and approved August 9, 2020 (received for review March 19, 2020)

Dynamic models of the protoplanetary disk indicate there should be large-scale material transport in and out of the inner Solar System, but direct evidence for such transport is scarce. Here we show that the $\epsilon^{50}\text{Ti}$ - $\epsilon^{54}\text{Cr}$ - $\Delta^{17}\text{O}$ systematics of large individual chondrules, which typically formed 2 to 3 My after the formation of the first solids in the Solar System, indicate certain meteorites (CV and CK chondrites) that formed in the outer Solar System accreted an assortment of both inner and outer Solar System materials, as well as material previously unidentified through the analysis of bulk meteorites. Mixing with primordial refractory components reveals a “missing reservoir” that bridges the gap between inner and outer Solar System materials. We also observe chondrules with positive $\epsilon^{50}\text{Ti}$ and $\epsilon^{54}\text{Cr}$ plot with a constant offset below the primitive chondrule mineral line (PCM), indicating that they are on the slope ~ 1.0 in the oxygen three-isotope diagram. In contrast, chondrules with negative $\epsilon^{50}\text{Ti}$ and $\epsilon^{54}\text{Cr}$ increasingly deviate above from PCM line with increasing $\delta^{18}\text{O}$, suggesting that they are on a mixing trend with an ordinary chondrite-like isotope reservoir. Furthermore, the $\Delta^{17}\text{O}$ -Mg# systematics of these chondrules indicate they formed in environments characterized by distinct abundances of dust and H₂O ice. We posit that large-scale outward transport of nominally inner Solar System materials most likely occurred along the midplane associated with a viscously evolving disk and that CV and CK chondrules formed in local regions of enhanced gas pressure and dust density created by the formation of Jupiter.

chondrules | bulk meteorites | isotope anomalies | disk transport | disk mixing

Chemical and isotopic signatures of primitive meteorites provide a powerful means to trace the earliest history of planet formation in our Solar System (1). Nucleosynthetic anomalies in ^{50}Ti and ^{54}Cr have been identified among major meteorite classes that distinguish planetary materials into two groups, noncarbonaceous and carbonaceous meteorites (2–5). Bulk meteorites and their components also show a significant variability in the mass-independent fractionation of O isotopes, which could have resulted from photochemical reactions that occurred heterogeneously across the protoplanetary disk (6). Several other isotope systems have now been found to show a similar dichotomy between noncarbonaceous and carbonaceous meteorites and, collectively, may not be easily explained by thermal processing of isotopically anomalous presolar carriers or addition of early-formed Ca- and Al-rich inclusions (CAIs) (7). Instead, most studies have proposed that the dichotomy was caused by spatial differences in isotopic signatures during the earliest stage of disk evolution (5, 7, 8), such that the isotopic signatures of noncarbonaceous and carbonaceous meteorites represent those of inner and outer disk materials, respectively.

Nucleosynthetic anomalies in ^{50}Ti and ^{54}Cr associated with bulk meteorites reflect the average composition of solids that were accreted onto their parent asteroids from local regions within the disk. However, local regions within the disk may

actually be composed of solids with diverse formation histories and, thus, distinct isotope signatures, which can only be revealed by studying individual components in primitive chondritic meteorites (e.g., chondrules). Chondrules are millimeter-sized spherules that evolved as free-floating objects processed by transient heating in the protoplanetary disk (1) and represent a major solid component (by volume) of the disk that is accreted into most chondrites. The nucleosynthetic anomalies in ^{50}Ti and ^{54}Cr of individual chondrules are, in most cases, similar to those of their bulk meteorites (9–12), which suggests a close relation between the regions where chondrules formed and where they accreted into their asteroidal parent bodies. However, exceptions to this observation are chondrules in CV chondrites, which display the entire range of ^{50}Ti and ^{54}Cr observed for all bulk meteorite groups (9, 11). Previous Cr isotope studies that have observed this larger isotopic range in CV chondrules have proposed that these chondrules or their precursor materials originated from a wide (not local) spatial region of the protoplanetary disk and were transported to CV chondrite accretion regions (9). In contrast, Ti isotope studies have suggested that the wide range of isotope anomalies observed in individual CV chondrules could

Significance

We present a coordinated petrologic, mineral chemistry, and multi-isotopic investigation of individual chondrules to further elucidate the origins and formation histories of planetary materials. We show chondrules from certain meteorites that accreted in the outer Solar System contain an assortment of both inner and outer Solar System material, as well as previously unidentified material. The outward transport of inner Solar System material places important constraints on dynamical models, as outward transport in the disk was thought possible only if significant barriers (e.g., Jupiter) to radial transport of materials do not exist. We show this “barrier” is either not completely impermeable to transport of millimeter-sized materials or additional mechanisms are required to transport materials to the outer Solar System.

Author contributions: Q.-Z.Y. designed research; C.D.W., M.E.S., C.D., Q.-Z.Y., N.T.K., D.S.E., A.Y., and K.Y. performed research; C.D.W., M.E.S., C.D., Q.-Z.Y., N.T.K., D.S.E., A.Y., and K.Y. analyzed data; and C.D.W., M.E.S., C.D., Q.-Z.Y., N.T.K., and D.S.E. wrote the paper.

The authors declare no competing interest.

This article is a PNAS Direct Submission.

This open access article is distributed under [Creative Commons Attribution-NonCommercial-NoDerivatives License 4.0 \(CC BY-NC-ND\)](https://creativecommons.org/licenses/by-nc-nd/4.0/).

¹To whom correspondence may be addressed. Email: cdwill@ucdavis.edu or qyin@ucdavis.edu.

²Present address: CAMECA, 92622 Gennevilliers Cedex, France.

³Present address: Center for Environmental Measurement and Analysis, National Institute for Environmental Studies, Tsukuba-City, 305-8506 Ibaraki, Japan.

This article contains supporting information online at <https://www.pnas.org/lookup/suppl/doi:10.1073/pnas.2005235117/-DCSupplemental>.

First published September 8, 2020.

be explained by the admixture of CAI-like precursor materials with highest nucleosynthetic ^{50}Ti and ^{54}Cr anomaly, which are abundant in CV chondrites (11).

Resolving these two competing interpretations would significantly improve our understanding of the origin of the isotopic dichotomy observed for bulk meteorites and provide constraints on the disk transport mechanism(s) responsible for the potential mixing of material with different formation histories. However, in earlier studies, Ti and Cr isotopes were not obtained from the same chondrules, which is required to uniquely identify their precursor materials and associated formation histories. Also absent in earlier studies is documentation of the properties (petrographic and geochemical) of individual chondrules that provide a valuable aid in interpreting Ti and Cr isotope data. Thus, we designed a coordinated chemical and Ti-Cr-O isotopic investigation of individual chondrules extracted from Allende (CV) and Karoonda (CK) chondrites (3). While the ^{50}Ti and ^{54}Cr of chondrules tracks the average composition of solids, the analyses of O isotopes and mineral chemistry of major Mg silicates (olivine and pyroxene) is useful to distinguish chondrules that are similar to those in ordinary chondrites (13–16) as well as precursor materials that may have formed in regions of the disk with variable redox conditions or with distinct proportions of

anhydrous dust versus H_2O ice (17). A significant number of high-precision Ti and Cr isotope analyses of bulk meteorites were also obtained for both carbonaceous and noncarbonaceous meteorites to help define the bulk meteorite ^{50}Ti - ^{54}Cr systematics of known planetary materials.

Results

Bulk Meteorite ^{50}Ti and ^{54}Cr Isotopes. We obtained analyses of Ti and Cr isotopic compositions (reported as $\epsilon^{50}\text{Ti}$ and $\epsilon^{54}\text{Cr}$, which are parts per 10,000 deviations from a terrestrial standard) for 30 bulk meteorites, all of which have mass-independent O isotope analyses reported as $\Delta^{17}\text{O}$ [a vertical deviation from the terrestrial fractionation line in parts per 1,000 (18)] previously reported (Dataset S1 and Fig. 1). The data clearly define two distinct isotopic groups: 1) noncarbonaceous meteorites, including enstatite chondrites (ECs), ordinary chondrites (OCs), and most differentiated meteorites known as achondrites (e.g., Moon, Mars, Vesta, angrites, ureilites, acapulcoites, lodranites, and winonaite) and 2) carbonaceous meteorites [including carbonaceous chondrites and several ungrouped achondrites (19)]. These two groups display orthogonal trends and are isolated from each other by a large area in $\epsilon^{50}\text{Ti}$ - $\epsilon^{54}\text{Cr}$ - $\Delta^{17}\text{O}$ isotope space that is devoid of any bulk meteorite compositions (shown

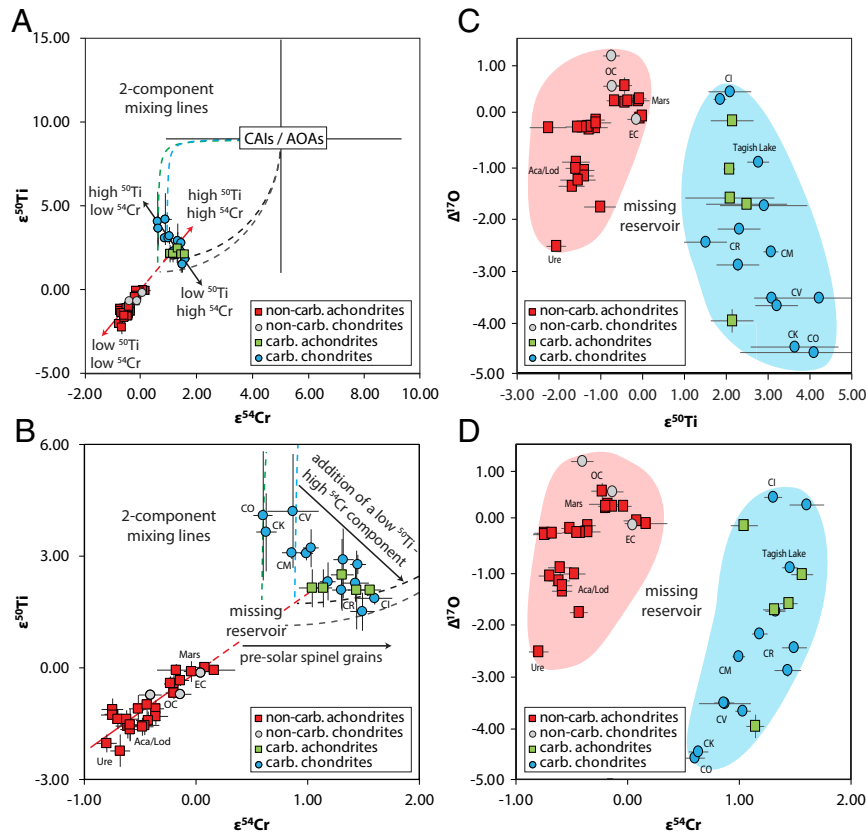


Fig. 1. The $\epsilon^{50}\text{Ti}$ - $\epsilon^{54}\text{Cr}$ - $\Delta^{17}\text{O}$ isotopic compositions of bulk carbonaceous and noncarbonaceous meteorites. (A,B) Data for $\epsilon^{50}\text{Ti}$ and $\epsilon^{54}\text{Cr}$ from this study are shown in Dataset S1. Literature data for $\epsilon^{50}\text{Ti}$ and $\epsilon^{54}\text{Cr}$ are from refs. 19–25. (C, D) Literature $\Delta^{17}\text{O}$ data are from refs. 26–42. Error bars are either the internal 2 SE or external 2 SD, whichever is larger. Note that noncarbonaceous meteorites are characterized by a strong positive linear correlation in the $\epsilon^{50}\text{Ti}$ - $\epsilon^{54}\text{Cr}$ - $\Delta^{17}\text{O}$ isotope space, while carbonaceous meteorites are characterized by a strong negative correlation in $\epsilon^{50}\text{Ti}$ - $\epsilon^{54}\text{Cr}$ (A, B) and $\epsilon^{50}\text{Ti}$ - $\Delta^{17}\text{O}$ (C) isotope spaces but a positive correlation in ^{54}Cr - $\Delta^{17}\text{O}$ (D) isotope space. Also shown (A) is the average $\epsilon^{50}\text{Ti}$ - $\epsilon^{54}\text{Cr}$ isotopic composition of “normal” CAIs. Error bars represent the overall range of reported normal CAI values. Dashed blue and green lines (A, B) represent a two-component mixing line between the average value of “normal” CAIs and extension of the noncarbonaceous line. Dashed black and gray lines represent a two-component mixing line between the average value of AOAAs and extension of the noncarbonaceous line. The red line represents a linear regression through noncarbonaceous meteorites, ostensibly inner Solar System materials (gray circles and red squares), calculated using Isoplot version 4.15. Note that the linear regression through noncarbonaceous meteorites intersects carbonaceous chondrite field near CM chondrites $\epsilon^{50}\text{Ti}$ - $\epsilon^{54}\text{Cr}$ isotope space (A, B). The “missing reservoir” denotes the region between noncarbonaceous and carbonaceous meteorite groups that lacks any reported bulk meteorite data. (B) Zoomed-in view of A. Legend abbreviations: carb., carbonaceous; noncarb., noncarbonaceous; EC, enstatite chondrite; OC, ordinary chondrite; Ure, ureilite; Aca/Lod (acapulcoite/lodranite).

as “missing reservoir” in Fig. 1). This paucity of samples remains even after including analyses from our expanded dataset. Previous work (2) calculated a linear regression through the non-carbonaceous meteorites using the data available at the time, which intersected the field defined by carbonaceous meteorites at approximately the composition of CI chondrites, an end-member of the carbonaceous meteorite field. However, when a linear regression is calculated through our expanded set of $\epsilon^{50}\text{Ti}$ and $\epsilon^{54}\text{Cr}$ of noncarbonaceous meteorites, the extrapolation of the regression intersects the middle of the bulk carbonaceous meteorite composition region, close to the CM chondrites and their immediate neighbors (Fig. 1B). This is markedly different from the previous study that proposed an intersection at one of the endmember locations of the carbonaceous region, near CI chondrites (2).

Mineral Chemistry and Textures of Selected Chondrules. The ferromagnesian chondrules studied here include porphyritic olivine (PO), porphyritic olivine-pyroxene (POP), and barred olivine (BO). Additionally, one chondrule from Allende is an Al-rich chondrule. The Mg# (defined as $\text{Mg\#} = [\text{MgO}]/[\text{MgO} + \text{FeO}]$ in molar percent) of Allende chondrules spans from 83 to 99.5 (Dataset S2). The olivine Cr_2O_3 content in the Allende chondrules in this study is mostly greater than 0.1%, which is different from the typically $<0.1\%$ Cr_2O_3 reported for Allende chondrules. Following the method of ref. 43, the average olivine Cr_2O_3 contents for seven Allende chondrules with forsterite (Mg_2SiO_4) content $\text{Fo} < 97$ is calculated to be $0.20 \pm 0.34 \text{ wt } \%$ (2 SD) (Dataset S6), which is similar to unequilibrated ordinary chondrites (UOCs) with subtype 3.1. It is likely that the large chondrules selected in this study (diameters of 2 to 3 mm; SI Appendix, Figs. S1 and S3) were less affected by thermal metamorphism than typical Allende chondrules. Three BO chondrules have Mg# 83 to 90, which are rare in CV chondrites (14,

16, 44), though they are similar to several FeO-rich BO chondrules studied for O isotopes by ref. 45. The Al-rich chondrule (Allende 4327-CH8) contains abundant Ca-rich plagioclase and zoned Ca-pyroxene. Chondrules in Karoonda are all olivine-rich and show homogeneous olivine compositions (Datasets S2 and S6). Their primary Mg# was subsequently modified during parent body metamorphism due to fast Fe–Mg exchange in olivine, though original porphyritic or barred olivine textures were preserved (SI Appendix, Figs. S2 and S4).

Multi-isotope Systematics of Individual Chondrules. The $\epsilon^{50}\text{Ti}$ and $\epsilon^{54}\text{Cr}$ analyses of individual chondrules in CV and CK chondrites show a large range from -2.3 to $+3.6$ and from -0.7 to $+1.2$, respectively (Datasets S2 and S3). These observed ranges are consistent with previous studies (2, 9–12) and span the entire range of isotopic compositions exhibited by bulk meteorite measurements. The Al-rich chondrule, Allende 4327-CH8, has an $\epsilon^{50}\text{Ti}$ value of $+8.4 \pm 0.3$, similar to the $\epsilon^{50}\text{Ti}$ observed in CAIs (2, 46). The $\epsilon^{54}\text{Cr}$ values of chondrules from CR, L, and EH chondrites show a narrow range within each meteorite and are consistent with those of bulk meteorites (Dataset S3), in contrast to the results from CV and CK chondrites.

Most chondrules (excluding Allende 4327-CH8) are internally homogenous with $\Delta^{17}\text{O}$ varying from -5‰ to 0‰ (Dataset S2). On a three-isotope diagram ($\delta^{17}\text{O}$ versus $\delta^{18}\text{O}$ in the Vienna Standard Mean Ocean Water scale where δ represents deviation from a standard in parts per 1,000; Fig. 2A), individual chondrules plot close to the primitive chondrule mineral (PCM) line (47) and are generally consistent with chondrules in CV chondrites (14, 16, 44, 45, 48, 49). Several FeO-rich BO chondrules plot very close to the terrestrial fractionation line, which is in good agreement with similar BO chondrules studied in refs. 16, 44, 45. Their O isotope ratios are similar to FeO-rich chondrules in Kaba by ref. 14 and Y-82094 (an ungrouped carbonaceous

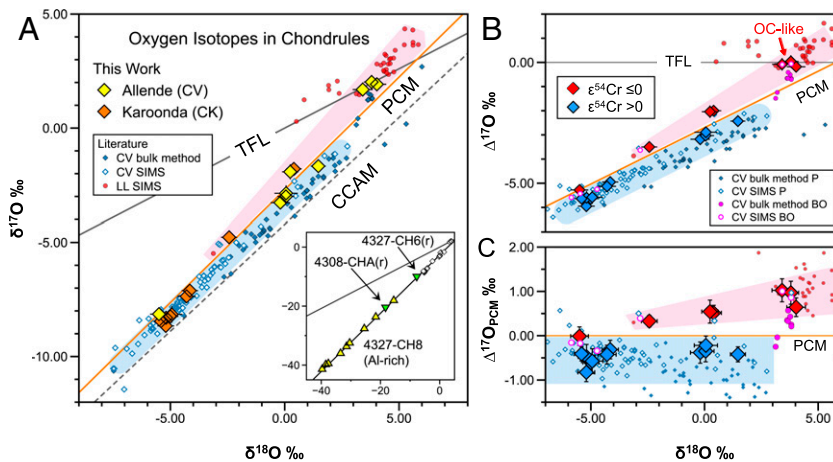


Fig. 2. Oxygen isotope ratios of chondrules from Allende and Karoonda meteorites with known ^{54}Cr and ^{50}Ti isotope anomalies. (A) Mean oxygen isotope ratios of individual chondrules from multiple SIMS analyses (Dataset S2). Terrestrial fractionation line (TFL; ref. 18), carbonaceous chondrite anhydrous mineral line (CCAM; ref. 52) and PCM line (47) are shown as reference. Oxygen isotope analyses of individual chondrules using bulk methods for CV (45, 48, 49), using SIMS for CV (14, 16, 44), and LL (50) are shown. Error bars are at 95% confidence level. Blue and pink shaded areas represent two linear trends among Allende and Karoonda chondrules, those that plot parallel to the PCM line along with the majority of literature CV chondrule data (blue) and those that plot toward LL chondrule data above the PCM line (pink). (Inset) The ^{16}O -rich relict olivine grains in Allende 4327-CH6 and 4308-CHA chondrules (green downward triangles) and individual data from Al-rich chondrule Allende 4327-CH8 (yellow upward triangles) that show heterogeneous oxygen isotope ratios (Dataset S4). For simplicity, only TFL and PCM line are shown in the inset. (B) Mass independent fractionation $\Delta^{17}\text{O}$ ($= \delta^{17}\text{O} - 0.52 \times \delta^{18}\text{O}$) of individual chondrules in Allende and Karoonda plotted against $\delta^{18}\text{O}$. Chondrules with negative $\epsilon^{54}\text{Cr}$ (red diamonds) plot above the PCM line toward LL chondrule data (pink shaded region), while those with positive $\epsilon^{54}\text{Cr}$ (blue diamonds) plot slightly below and parallel to the PCM line, along with majority of CV chondrules in the literature (blue shaded region). Three BO chondrules plotted on TFL are regarded as ordinary chondrite-like chondrules. Literature data of BO chondrules in CV (open and filled pink circles using bulk methods and SIMS) often show oxygen isotope ratios above the PCM line. (C) Deviation of $\Delta^{17}\text{O}$ relative to the PCM line ($\Delta^{17}\text{O}_{\text{PCM}} = \delta^{17}\text{O} - 0.987 \times \delta^{18}\text{O} + 2.70$). Chondrules with positive $\epsilon^{54}\text{Cr}$ show a constant offset from the PCM line ($\sim -0.5\text{‰}$), indicating that they are on the slope ~ 1.0 in the oxygen three-isotope diagram. In contrast, chondrules with negative $\epsilon^{54}\text{Cr}$ (and $\epsilon^{50}\text{Ti}$) increasingly deviate from the PCM line with increasing $\delta^{18}\text{O}$, suggesting that they are on the mixing trend with an ordinary chondrite-like isotope reservoir.

chondrite) by ref. 13, which are considered to have ordinary chondrite chondrule-like O isotope ratios (50). The Al-rich chondrule Allende 4327-CH8 is the only chondrule in this study that showed significant internal heterogeneity in O isotopes, with $\delta^{17,18}\text{O}$ values approaching $\sim -40\text{‰}$ (Fig. 2A, Inset), the lowest values of which are close to those observed for CAIs and amoeboid olivine aggregates (AOAs) (51). Fig. 2 shows that, in detail, many chondrules in this study as well as CV chondrules in the literature plot slightly below the PCM line, while others including FeO-rich BO chondrules plot above the PCM line and trend toward ordinary chondrite chondrule data (50). This small difference becomes a more notable division when chondrules are sorted by their $\epsilon^{50}\text{Ti}$ or $\epsilon^{54}\text{Cr}$ (Fig. 2B and C); chondrules above the PCM line all have negative $\epsilon^{54}\text{Cr}$, and those below the PCM line have positive $\epsilon^{54}\text{Cr}$ (Fig. 2B and C). It should be noted, however, that this division about the PCM line cannot be universally applied to the bulk meteorites data as ureilites, for example, which have negative $\epsilon^{50}\text{Ti}$ and $\epsilon^{54}\text{Cr}$ isotopic compositions, plot well below the PCM line.

By combining Ti-Cr-O isotope systems of Allende and Karoonda chondrules (Figs. 3 and 4), these chondrules are grouped into three general “clusters” that display distinct isotope signatures: 1) similar to bulk carbonaceous meteorites, 2) within noncarbonaceous meteorite field, and 3) near the missing reservoir with slightly positive $\epsilon^{50}\text{Ti} \sim +1$ to 2, $\epsilon^{54}\text{Cr} \sim 0$, and $\Delta^{17}\text{O} \sim -5\text{‰}$. Such distinct groups cannot be identified from a single isotope system. Although the total ranges of $\epsilon^{50}\text{Ti}$ and $\epsilon^{54}\text{Cr}$ are slightly smaller for chondrules in Karoonda than those in Allende, both chondrule datasets vary similarly in multi-isotope systematics, suggesting that both Ti and Cr in the bulk chondrules and olivine O isotopes retained their primary isotope signatures even with the mild metamorphic conditions experienced by CK4 chondrites. The Al-rich chondrule (Allende 4327-CH8) shows an intermediate Ti and Cr isotopic composition, which may be caused by the mixing of CAI-like precursors in the chondrule (2), consistent with its Al-rich mineralogy and low $\delta^{18}\text{O}$ and $\delta^{17}\text{O}$ values approaching those of CAIs (Figs. 3A and 4C and D).

Discussion

Mixing Model and the Missing Reservoir. The distinct grouping of noncarbonaceous and carbonaceous meteorites in $\epsilon^{50}\text{Ti}$ - $\epsilon^{54}\text{Cr}$ space was proposed to result from the addition of refractory inner Solar System dust such as CAIs to CAI-free outer Solar System matrix, as represented by CI chondrites (2). This two-component mixing (2) is predicated on a regression line intersecting the carbonaceous meteorite trend at the bulk, CAI-free CI chondrite composition (2). However, with our newly acquired bulk meteorite data (Dataset S1), Fig. 1 reveals that an updated linear extrapolation of only the noncarbonaceous meteorites intersects the middle of the region defined by the bulk carbonaceous meteorites, close to CM chondrites and their immediate neighbor, but not CI chondrites, which was a requirement of previous models (2).

Importantly, theoretical mixing trajectories of noncarbonaceous endmembers with CAI-like dust (2) do not allow the resulting isotopic compositions for bulk carbonaceous meteorites to plot below the linear extrapolation of the noncarbonaceous meteorites (Figs. 1 and 3). Therefore, adding CAI-like components to the linear noncarbonaceous trend (2, 11) cannot account for the entire carbonaceous chondrite trend (which includes most CR chondrites, CI and CB chondrites, and Tagish Lake). Rather, carbonaceous members that plot below the noncarbonaceous extension line (Figs. 1 and 3) require mixing either with AOA-like materials that are characterized by positive $\epsilon^{50}\text{Ti}$ and $\epsilon^{54}\text{Cr}$ values (e.g., forsterite-bearing CAIs like SJ101; ref. 53) with relatively low Ti/Cr ratios or a hypothetical presolar component characterized by a relatively low $\epsilon^{50}\text{Ti}$ and high $\epsilon^{54}\text{Cr}$

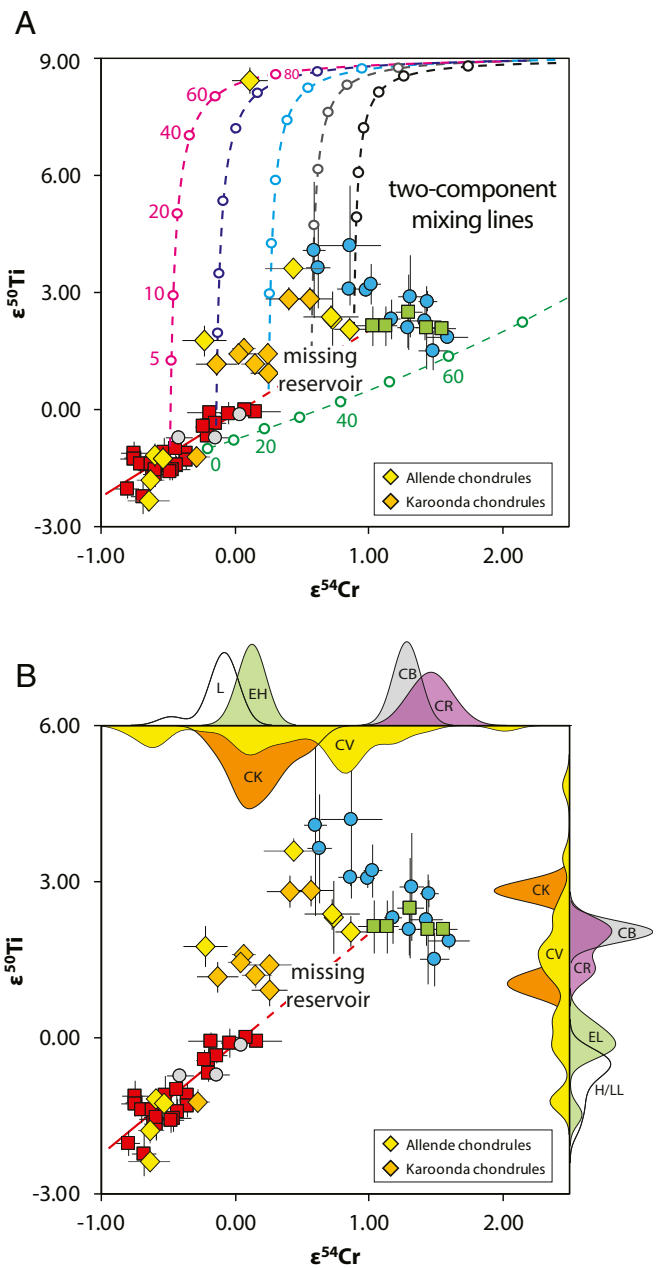


Fig. 3. The $\epsilon^{50}\text{Ti}$ - $\epsilon^{54}\text{Cr}$ isotopic compositions of individual chondrules. (A) The $\epsilon^{50}\text{Ti}$ - $\epsilon^{54}\text{Cr}$ isotopic compositions of bulk meteorites (Fig. 1) and individual chondrules from CV (Allende; yellow diamonds) and CK (Karoonda; orange diamonds) chondrites. Bulk meteorite symbols are the same as in Fig. 1. Error bars are either the internal 2 SE or external 2 SD, whichever is larger. Each of the multicolored dashed lines with tick marks represents a two-component mixing line between either the average value of “normal” CAIs (the five concave down curves) or AOAs with relatively low Ti/Cr ratios (the green semilinear curve) and members of the extended noncarbonaceous meteorite group (Fig. 1). Note that these mixing lines project to an endmember characterized by an inner Solar System noncarbonaceous composition that extends to and bridges the carbonaceous chondrite field, filling the “missing reservoir” shown in Fig. 1. (B) Zoomed-in view of A. Also shown are kernel density plots of individual chondrules including our data here as well as literature data (2, 9–12) constructed using the MATLAB ksdensity function with bandwidths of 0.2 and 0.1 for $\epsilon^{50}\text{Ti}$ and $\epsilon^{54}\text{Cr}$ isotopic compositions, respectively. Note the limited range in $\epsilon^{50}\text{Ti}$ - $\epsilon^{54}\text{Cr}$ isotopic compositions of individual chondrules from CR, CB, enstatite, and ordinary chondrites (outside Fig. 2B axes) relative to chondrules from CV and CK chondrites (inside Fig. 2B axes). Data obtained from this study are shown in Datasets S1–S3.

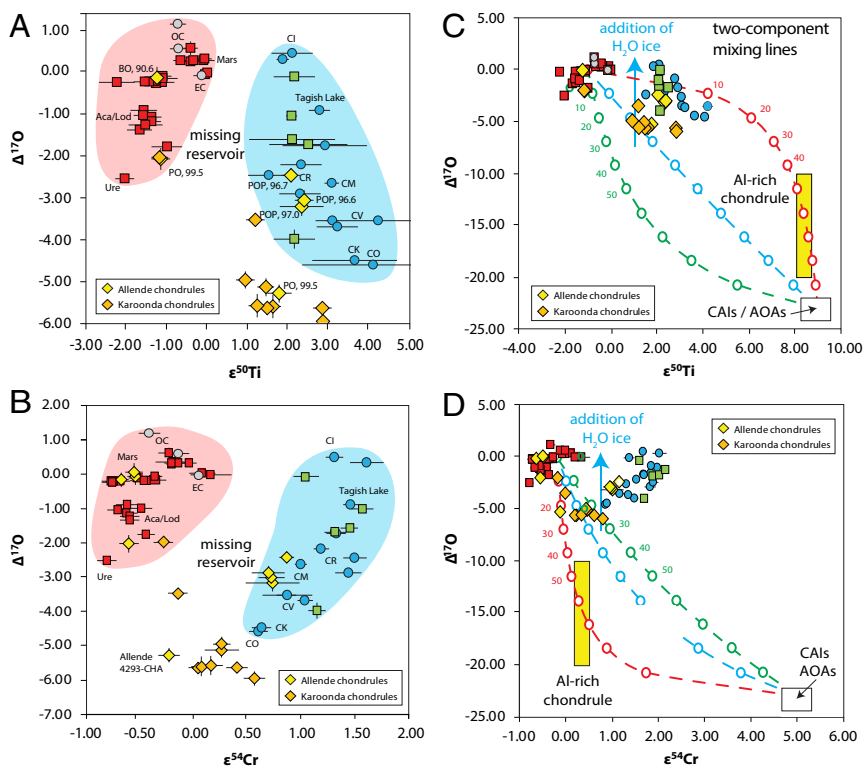


Fig. 4. The $\epsilon^{50}\text{Ti}$ - $\epsilon^{54}\text{Cr}$ - $\Delta^{17}\text{O}$ isotopic compositions of bulk meteorites and individual chondrules. The $\epsilon^{50}\text{Ti}$ - $\Delta^{17}\text{O}$ (A and C) and $\epsilon^{54}\text{Cr}$ - $\Delta^{17}\text{O}$ (B and C) isotope systematics of bulk meteorites (see Fig. 1) and individual chondrules from CV (Allende) and CK (Karoonda) chondrites. Color symbols are the same as in Fig. 1. Error bars are either the internal 2 SE or external 2 SD, whichever is larger. Several individual chondrules are characterized by isotopic compositions that plot within the missing reservoir or outside the regions defined by noncarbonaceous and carbonaceous meteorites. (C and D) Zoomed-out views of A and B. The $\Delta^{17}\text{O}$ isotopic composition of the Al-rich chondrule from Allende (4327-CH8) is variable S4 (Dataset S4) and therefore displayed as a yellow bar covering the entire range. Also labeled is Allende chondrule 4293-CHA. The red curve represents mixing with a "typical" CAI Ti/Cr ratio as one endmember (though this could also be an AOA depending on what that AOA is actually composed of). The blue curve represents mixing with a "typical" AOA Ti/Cr ratio as one endmember (though this could also be a CAI depending on what that CAI is actually composed of). The green curve represents mixing with an "olivine-rich" AOA with elevated Cr contents as one endmember. These three curves show that the vast majority of our "intermediate" chondrule data can be explained by mixing "average" noncarbonaceous material with either CAIs or AOAs, while the rest of our chondrules could just be reprocessed carbonaceous or noncarbonaceous materials.

values. Future work should continue to search for possible pre-solar materials that may be characterized by depleted $\epsilon^{50}\text{Ti}$ and enriched $\epsilon^{54}\text{Cr}$ signatures. This component of the carbonaceous meteorite trend may also reflect the addition of Cr-rich spinel grains that are characterized by large excesses in $\epsilon^{54}\text{Cr}$ (e.g., ref. 54) to materials that lie on the extension of the noncarbonaceous line. In this scenario, bulk meteorite values would shift horizontally (because spinel contains a negligible amount of Ti) to this region of carbonaceous materials.

The wide range in the isotopic composition of individual chondrules from Allende and Karoonda demonstrates that these chondrules formed from a variety of materials including noncarbonaceous meteorite-like dust, carbonaceous meteorite-like dust, CAI- or AOA-like dust, and dust from a reservoir with intermediate $\epsilon^{50}\text{Ti}$ and $\epsilon^{54}\text{Cr}$ values that is not apparent from the analysis of only bulk meteorites (Figs. 1, 3, and 4). A single Al-rich chondrule (4327-CHA) is a prime example of a mixture between (75%) CAIs and (25%) noncarbonaceous materials, characterized by excesses in both $\epsilon^{50}\text{Ti}$ and $\epsilon^{54}\text{Cr}$ isotopic compositions of 8.42 and 0.11, respectively (Fig. 3A). Significant addition of a CAI precursor component to this chondrule is also evident from abundant ^{16}O -rich relict olivine grains in this Al-rich chondrule that show variable $\Delta^{17}\text{O}$ values from -10% down to -21% , similar to those of CAIs (Figs. 2A, Inset and 4C and D and Dataset S4). Mixing between CAIs and less refractory materials is also consistent with observations of relict CAIs inside

chondrules (55–57) and the extremely low $\Delta^{17}\text{O}$ values of some chondrule spinel grains (13, 58, 59) as well as the texture and chemical composition of relict grains with surrounding chondrule glass (60, 61).

Several chondrules from both CV and CK chondrites that have intermediate $\epsilon^{50}\text{Ti}$ and $\epsilon^{54}\text{Cr}$ values and lie slightly above the linear extrapolation of the noncarbonaceous field (e.g., Fig. 3A) may reflect two-component mixing between either CAIs or AOA-like precursors and the extended noncarbonaceous reservoir (Fig. 3A). AOAs are inferred to have formed from the same isotopic reservoirs as CAIs (e.g., ref. 51) but are less refractory than CAIs, meaning lesser amount of Ti but more Cr than CAIs (62). The mixing trajectory with AOAs should result in a mixing line with a lower or even an opposite curvature compared to that of CAIs depending in the exact nature of the Ti/Cr ratios (Figs. 1A and B, 3A, and 4C and D). Although the $\epsilon^{50}\text{Ti}$ and $\epsilon^{54}\text{Cr}$ values of AOAs have not been measured, it is reasonable to assume AOAs have $\epsilon^{50}\text{Ti}$ and $\epsilon^{54}\text{Cr}$ composition similar to that of CAIs (including forsterite-bearing CAIs; 53) given that AOAs and CAIs are observed to have similar $\Delta^{17}\text{O}$ values (51). AOAs are abundant in CV chondrites and are often considered to be precursors of chondrules that contain ^{16}O -rich relict olivine (e.g., ref. 63). Based upon the observations that the majority of chondrules in the CV chondrites plot on mixing lines between materials of non-carbonaceous composition and the more refractory CAI and AOA-like compositions (Figs. 3 and 4),

it can be inferred that the vast majority of CV chondrite chondrules are representative of mixtures of at least two distinct precursor reservoirs.

Thermal Processing and Unmixing? Our results indicate the non-carbonaceous trend is unlikely related to thermal processing (often referred to as “unmixing”) of isotopically distinct dust (2, 9). For thermal processing to result in the linear trend observed for the noncarbonaceous meteorites, the elemental Ti/Cr ratios of the dust being processed would have to remain unfractionated. However, Ti and Cr are characterized by very different volatilities and carrier phases, and therefore thermal processing of dust is unlikely to result in the linear trend in $\epsilon^{50}\text{Ti}$ and $\epsilon^{54}\text{Cr}$ space. Bulk carbonaceous and noncarbonaceous materials also display a continuum in their $\Delta^{17}\text{O}$ values, that is, their $\Delta^{17}\text{O}$ values overlap each other and lack any indication of clustering into distinct $\Delta^{17}\text{O}$ groups (Fig. 1 C and D). This demonstrates that, while the variability observed in the $\epsilon^{50}\text{Ti}$ - $\epsilon^{54}\text{Cr}$ isotopic compositions of bulk meteorites is due to dust that accreted to form planetesimals, the $\Delta^{17}\text{O}$ values reflect additional components that did not significantly affect $\epsilon^{50}\text{Ti}$ - $\epsilon^{54}\text{Cr}$ isotopic compositions (e.g., H_2O ice, hydrated minerals, and organics).

Chondrule Formation Environment. Allende chondrules show a range of diversity in both Mg# and $\Delta^{17}\text{O}$ (Fig. 5 and [Datasets S2](#) and [S4](#)) similar to those of CV and other carbonaceous chondrites, such as Y-82094 and Kaba (13, 14). By adapting a mass balance model for chondrule O isotope under the existence of ^{16}O -poor H_2O ice in carbonaceous chondrite-forming regions (14, 17), the formation environment of each chondrule can be estimated. One Allende chondrule (Allende 4293-CHA) is characterized by a Mg# ~ 99.5 and $\Delta^{17}\text{O} \sim -5.3\text{‰}$ (Fig. 5), which corresponds to an environment with relatively low dust enrichment and an abundance of ^{16}O -poor H_2O ice associated with its precursor materials (≤ 100 times Solar and ≤ 0.6 times CI, respectively; ref. 14). Chondrules with high Mg# (>98) and $\Delta^{17}\text{O} \sim -5\text{‰}$ are the most common type of chondrules in CV chondrites (14, 16) (also in [SI Appendix, Fig. S5](#)). The same chondrule (Allende 4293-CHA) has isotopic values of $\epsilon^{50}\text{Ti} = 1.8$ and $\epsilon^{54}\text{Cr} = -0.2$, which fall between the noncarbonaceous and carbonaceous groups (Fig. 3), where no bulk meteorite data were previously observed. Chondrules with positive $\epsilon^{50}\text{Ti}$ and $\epsilon^{54}\text{Cr}$ values, similar to bulk carbonaceous meteorites, have lower

Mg# ~ 97 and $\Delta^{17}\text{O} \sim -3\text{‰}$ (Fig. 5), consistent with a formation environment characterized by higher abundances of H_2O ice (~ 0.8 times CI) with relatively higher dust enrichments (100 to 200 times Solar).

Other Allende chondrules with higher $\Delta^{17}\text{O}$ (-2 to 0‰) are those with negative $\epsilon^{50}\text{Ti}$ and $\epsilon^{54}\text{Cr}$ values. They plot above the model curve for the CI chondritic H_2O ice abundance (4 times CI) and at low to relatively high dust enrichments (~ 20 times Solar for Allende 4327-CH6 and approaching ~ 500 times Solar for BO chondrules). However, their O isotopic compositions are fractionated above the PCM line (Fig. 2 B and C) toward the region occupied by ordinary chondrites (50), which may represent mixing with ordinary chondrite-like dust, but not with ^{16}O -poor H_2O ice as in the model assumption. If these chondrules were formed in the environments similar to those of ordinary chondrite chondrule formation, the mass balance model in Fig. 5 may not be relevant to estimate the ice enhancement factor and would have higher dust-enrichment factors than the estimates (*Methods*).

Radial Transport in the Protoplanetary Disk. Our data suggest that CV and CK chondrites, which are interpreted to have accreted in the outer Solar System (5), collected materials that originated from a variety of Solar System reservoirs, as evidenced by the Ti and Cr isotopic composition of their constituent chondrules. It has been proposed that radial transport of materials from the inner to outer Solar System may occur in viscously evolving disks, where flow along the disk midplane (also known as meridional flow) transports inner Solar System dust to larger orbital distances (64–67), as far out as the Kuiper Belt, before slowly drifting back toward the Sun. The outward transport of inner Solar System dust in viscously evolving disks is only possible if significant barriers to radial transport of materials (e.g., gaps and pressure bumps) do not exist; for example, giant planets such as Jupiter have yet to grow to sufficient size to limit diffusive transport between the inner and outer Solar System along the disk midplane. Once Jupiter formed, inner Solar System dust previously transported to the outer Solar System could have become trapped while remaining inner Solar System materials would have been prevented from any further transport beyond Jupiter (64, 68, 69).

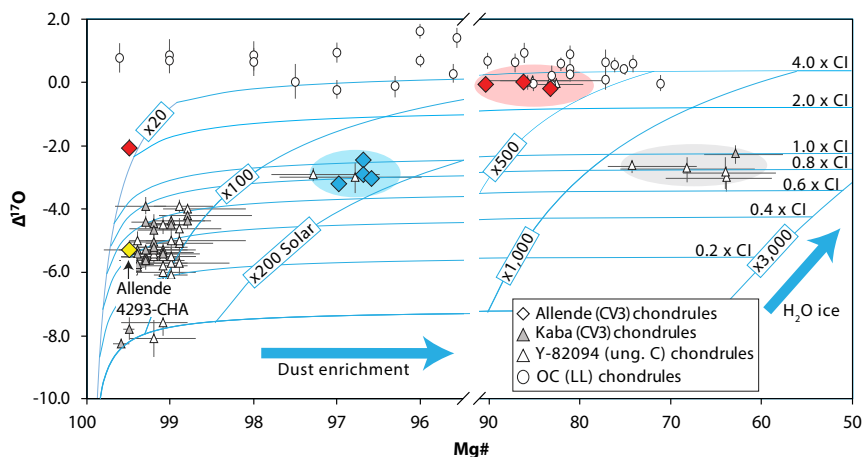


Fig. 5. Oxygen isotope ratios of Allende chondrules versus their Mg#. Chondrules from Allende (CV3) (this study), Kaba (CV3) (14), ungrouped Y-82094 (13), and (LL) ordinary chondrites (50) Bishinpur, Semarkona, and Krymka are plotted. Curves are from the O isotope mixing model with variable ratios of water ice enhancement factors relative to CI chondritic proportions and under variable dust enrichment factors relative to Solar abundance. See *Methods* for more details about the mixing model. Allende chondrule data with noncarbonaceous, carbonaceous, or missing reservoir $\epsilon^{50}\text{Ti}$ - $\epsilon^{54}\text{Cr}$ signatures are represented by red, blue, and yellow diamonds, respectively. These chondrules as well as majority of chondrules from other CV3 chondrites plot along the model curves, suggesting that they formed in the environments with variable ^{16}O -poor water ice and dust enrichment.

Jupiter Maintains the Great Isotopic Dichotomy. In this scenario, if the inner Solar System had become devoid of CAIs [having been accreted onto the Sun or transported beyond Jupiter (64)], then meteorites like ordinary and enstatite chondrites forming inside of Jupiter's orbit would primarily accrete material defining a very narrow range in their $\epsilon^{50}\text{Ti}$ - $\epsilon^{54}\text{Cr}$ - $\Delta^{17}\text{O}$ -Mg# compositions (e.g., ordinary and enstatite chondrite chondrules). The dust in this region would be characterized by deficits in $\epsilon^{50}\text{Ti}$ and $\epsilon^{54}\text{Cr}$ that is accompanied by a relatively high but still limited range in $\Delta^{17}\text{O}$ (similar to chondrules from ordinary chondrites). Alternatively, the relatively high $\Delta^{17}\text{O}$ values could have resulted from interactions with H_2O ice transported inward prior to the formation of Jupiter.

In contrast, carbonaceous chondrites meteorites that formed just outside of Jupiter's orbit (e.g., CV and CK parent bodies) could have accreted inner Solar System dust, CAI- and/or AOA-like dust, and less refractory outer Solar System material (64, 70). If this is correct, chondrules that formed from dust in this region would then display a very broad range in their observed $\epsilon^{50}\text{Ti}$ - $\epsilon^{54}\text{Cr}$ - $\Delta^{17}\text{O}$ isotopic compositions, for example as seen in the Allende and Karoonda chondrules, where the resulting composition depends on the relative proportion of inner versus outer Solar System materials incorporated into each individual chondrule. A pressure maximum just outside the orbit of Jupiter could also have trapped locally variable amounts of ^{16}O -poor H_2O ice, resulting in chondrule formation under variable redox conditions. Incorporation of this H_2O ice during chondrule formation would not only increase the bulk $\Delta^{17}\text{O}$ value of a chondrule but also lower its bulk Mg#, due to oxidation of Fe to FeO (Fig. 5).

Permeable Barrier and Crossing the Gap. Al-Mg ages of ordinary chondrite-like chondrules in Acfer 094 (a most primitive carbonaceous chondrite) suggest these chondrules formed in inner disk regions 1.8 My after CAIs and more than 0.4 to 0.8 My prior to the rest of the chondrules in the same meteorite (15). The discovery of noncarbonaceous-like chondrules and their mixing with CAIs and/or AOAs in CV chondrites in this study, together with chondrules from Acfer 094, collectively suggest transport from the inner to the outer Solar System was a far more frequent and protracted processes. Outward transport is not limited to just CAIs and AOAs at the earliest stages of disk evolution. This delayed timing (>1.8 My after CAIs) of outward transport of ordinary chondrite-like, inner Solar System material is interesting as it has been proposed that Jupiter formed in less than 1 My (8); if ordinary chondrite-like chondrules were transported from the inner to the outer Solar System after this time then it means either the formation of Jupiter did not create a barrier completely impermeable to outward flow along the midplane at this time (at least for materials of this size with diameters of ~2 to 3 mm) or some material was transported above this barrier by disk winds. An alternative to gap permeability is that our understanding of chondrule chronology is in question due to potential heterogeneity of ^{26}Al distribution in the early Solar System allowing age uncertainties up to two half-lives of ^{26}Al (cf. figure 6 in ref. 19).

The dust farther out in the Solar System than CV and CK parent bodies displays a relatively narrow range in $\epsilon^{50}\text{Ti}$ - $\epsilon^{54}\text{Cr}$, perhaps similar to that observed for CR chondrite chondrules (Fig. 3B; ref. 9 and this study). Chondrules from CR chondrites (17) also show systematically lower Mg# and higher $\Delta^{17}\text{O}$ values than those in CV chondrites (14, 16), most likely due to enhancement of ^{16}O -poor H_2O ice in the outer Solar System. What distinguishes CR chondrites from other carbonaceous chondrites is that their parent body formed late, greater than 4 My after CAIs, as indicated from many chondrules with no resolvable ^{26}Mg excess (70). Chondrite parent bodies in the inner disk were likely formed by ~2.5 Ma (64), when transport of noncarbonaceous

chondrules to the outer disk would have stopped. Therefore, it is likely that CR chondrite accreted largely carbonaceous chondrules of local origin after ~4 Ma in the outer Solar System, and almost no noncarbonaceous chondrules accreted into the CR chondrite parent body.

Our results, which link Ti, Cr, and O isotope systematics with the mineral chemistry of chondrules, reveal that, in the context of current dynamical models, large-scale outward transport of inner Solar System materials occurred in the protoplanetary disk, resulting in complex mixing of multiple components in the accretion region of some chondrite parent bodies.

Methods

Selections of Chondrules for Isotope Analyses. Ten chondrules from Allende (CV3) and nine chondrules from Karoonda (CK4) were selected for coordinated isotopic (Cr, Ti, and O), petrologic, and mineral chemistry analyses (Datasets S2, S4, S5, and S6), together with 31 bulk rock carbonaceous and noncarbonaceous chondrites and achondrite meteorites (Dataset S1). An additional 28 chondrules from Allende (CV3), EET 92048 (CR2), Xinglongquan (L3), and Qingzhen (EH3) were analyzed for Cr isotopes (Dataset S3), which include three Allende chondrules that were also analyzed for Ti isotopes (Dataset S2). The mean diameters of chondrules in CV and CK chondrites are typically ~900 μm and indistinguishable between CV and CK (71). For the purpose of obtaining enough Cr and Ti for isotopic analyses, large Allende chondrules with diameters of 1.5 mm to 3 mm were used. Diameters of Karoonda chondrules used in this work are also relatively larger than mean diameters, from 1 mm to 1.5 mm. While both Allende and Karoonda meteorites experienced mild thermal metamorphism in their parent bodies with petrologic types of 3.6 and 4, respectively, both Cr and Ti isotopes in these relatively large chondrules should be preserved within each chondrule against diffusional exchange in their parent bodies. All of these chondrules were scanned individually at high resolution using computed tomography at the Advanced Photon Source, Argonne National Laboratory. The selected chondrules were broken in two; one half was mounted in an epoxy thick section and the other half (3 to 27 mg) was used for Cr and Ti isotope analyses.

Major Element Analyses. Electron microprobe analysis (EPMA) maps were acquired at the American Museum of Natural History (AMNH) using epoxy sections for 19 chondrules in Allende and Karoonda (Datasets S2 and S6). Additional data are curated as part of the AMNH meteorite collection (<http://digitalibrary.amnh.org/handle/2246/6952>). X-ray mapping, and analyses of silicates and metal grains were performed for 19 chondrules in Allende and Karoonda using the five-spectrometer CAMECA SX100 electron probe microanalyzer at AMNH. Maps 512×512 pixels in size were acquired for Na, Mg, Al, Si, S, Ca, Fe, and Ni, as well as the back-scattered electron signal, in stage mode with 1- μm beam, 3- to 5- μm step, and typically 20-ms dwell time per pixel. Combined elemental maps with virtual colors, such as Mg-Ca-Al for red-green-blue, are examined and used to identify phases and their two-dimensional mode in each chondrule, including olivine, high-Ca and low-Ca pyroxene, feldspar, spinel, mesostasis, metal, and sulfide.

Ti and Cr Isotope Analyses. Material for bulk isotopic analyses were prepared from interior, fusion-crust free chips of each sample. Interior chips ranging in mass from 10 to 100 mg were gently crushed and homogenized in an agate mortar and pestle. An aliquot (ranging from 10 to 30 mg for bulk meteorites and 3 to 27 mg for chondrules) of the homogenized powders were placed in polytetrafluoroethylene (PTFE) Parr capsules along with a 3:1 mixture of ultraclean HF:HNO₃. The PTFE capsule was placed into a stainless-steel jacket and heated in an oven at 190 °C for 96 h. This high-temperature pressure dissolution procedure ensures digestion of all phases, including refractory phases such as chromite and spinel. After dissolution, the sample solution was dried down and treated by alternating 6 M HCl and concentrated HNO₃ to break down any fluorides formed during the dissolution process. The sample was then brought back up in 1 mL of 6 M HCl for the Cr separation chemistry using the procedure previously described by ref. 72. This chemical separation procedure utilizes a sequential three-column procedure (one anion resin column followed by two cation resin columns). After Cr was removed from the sample matrix, the remaining material were then processed through a sequence of columns to isolate Ti following the procedure described by ref. 73. The Ti yields after processing through the entire column procedure were >98%. All chemical separation was completed in a clean laboratory facility at the University of California, Davis (UC Davis).

Chromium isotopic ratios were determined using a Thermo Triton Plus thermal ionization mass spectrometer at UC Davis. Purified Cr was loaded onto outgassed tungsten filament with a load of 1 to 3 μg per filament depending on the amount of Cr available from the sample. The Cr was loaded across four filaments for a total load of 4 to 12 μg of Cr. The four sample filaments were bracketed by four filaments (two before and two after) loaded with the NIST SRM 979 Cr standard with the same loading amount as the sample. Each filament run consists of 1200 ratios with 8-s integration times. Signal intensity of ^{52}Cr was set to 10, 8, or 6 V ($\pm 10\%$) for 3-, 2-, and 1- μg Cr loads, respectively. A baseline was measured every 25 ratios along with a rotation of the amplifiers. A gain calibration was completed at the start of every filament. Instrumental mass fractionation was corrected for using an exponential law and a $^{50}\text{Cr}/^{52}\text{Cr}$ ratio of 0.051859 (74). The $^{54}\text{Cr}/^{52}\text{Cr}$ ratios are expressed in parts per 10,000 deviation (ϵ -notation) from the measured NIST SRM 979 standard as $\epsilon^{54}\text{Cr}$.

Titanium isotopic ratios were measured using a Thermo Neptune Plus multicollector inductively coupled plasma mass spectrometer (MC-ICPMS) at UC Davis. Samples were introduced into the MC-ICPMS using a Nu Instruments DSN-100 desolvating nebulizer. The interface was equipped with a standard H-type skimmer cone and a Jet-style sample cone. Typical intensity for ^{48}Ti was 25 V using a 10^{11} -ohm resistor for a 1-ppm solution run in high-resolution mode. The isotope ratios were measured in a multidynamic routine with $^{44}\text{Ca}^+$, $^{46}\text{Ti}^+$, $^{47}\text{Ti}^+$, $^{48}\text{Ti}^+$, $^{49}\text{Ti}^+$, and $^{50}\text{Ti}^+$ in step 1 and $^{49}\text{Ti}^+$, $^{51}\text{V}^+$, and $^{53}\text{Cr}^+$ in step 2. Ratios were internally normalized to a $^{49}\text{Ti}/^{47}\text{Ti}$ ratio of 0.749766 (75). The $^{50}\text{Ti}/^{47}\text{Ti}$ ratios are expressed in parts per 10,000 deviation (ϵ -notation) from the Ti terrestrial standard as $\epsilon^{50}\text{Ti}$.

SIMS O Isotope Analyses. The O isotopic composition of olivine and pyroxene phenocrysts in chondrules from minimally thermally and aqueously altered meteorites is indistinguishable from that of the glassy mesostasis (e.g., ref. 47). However, glass and plagioclase in chondrules from most unequilibrated chondrites are different from those of olivine and pyroxene phenocrysts due to low-temperature O isotope exchange with ^{16}O -poor fluid (16, 44, 50). Due to extremely slow O isotope diffusion rates of olivine and pyroxene, they preserve the O isotope signature at the time of chondrule formation even in type 4 chondrites (76). Thus, we have analyzed the O isotope ratios of olivine or pyroxene phenocrysts by using secondary ion mass spectrometer (SIMS) in chondrules from Allende (CV3) and Karoonda (CK4) to represent their primary O isotope signatures.

Nineteen chondrules from Allende and Karoonda were remounted into eight 25-mm round epoxy sections with San Carlos olivine standard (SC-OI, 51) grains for the SIMS O isotope analyses at the University of Wisconsin–Madison. This was done to ensure the best-quality O three-isotope analyses. As many as three chondrules were mounted together in a single epoxy mount. Scanning electron microscope images were obtained for remounted samples using the Hitachi S-3400N at the University of Wisconsin–Madison prior to SIMS analyses. Eight olivine and/or pyroxene grains per chondrule were selected for SIMS analyses. For each grain, semiquantitative energy-dispersive X-ray spectroscopy analyses were acquired (15 keV, 30-s detection time) and applied for matrix corrections during SIMS analyses (discussed below). In the case of BO and PO chondrules, all grains selected were olivine, while a representative selection of both pyroxene and olivine was determined for POP chondrules.

Oxygen three-isotope analyses were performed using the IMS 1280 at the WiscSIMS laboratory under multicollector Faraday cup detections (13–17, 44, 47, 50). The Cs^+ primary beam was set to ~ 12 - μm diameter and 3-nA intensity, which resulted in secondary $^{16}\text{O}^-$ intensities of $\sim 3.5 \times 10^9$ counts per second. The contribution of tailing $^{16}\text{O}^1\text{H}^-$ ions on the $^{17}\text{O}^-$ signal was negligible ($< 0.1\%$). Each single spot analysis took 7 min, with a typical external precision of $\sim 0.3\%$, $\sim 0.4\%$, and $\sim 0.4\%$ (2 SD) for $\delta^{18}\text{O}$, $\delta^{17}\text{O}$, and $\Delta^{17}\text{O}$ ($= \delta^{17}\text{O} - 0.52 \times \delta^{18}\text{O}$), respectively. The mass resolving power (MRP at 10% peak height) was set at $\sim 5,000$ for ^{17}O and $\sim 2,200$ for ^{16}O and ^{18}O . Instrumental biases of olivine and pyroxene relative to the SC-OI standard were calibrated using multiple standards (Fo_{60} , Fo_{100} , En_{85} , En_{97} , and diopside) with known O isotope ratios that cover the range of compositions of the unknowns (50). The results are presented in [Datasets S2, S4, and S5](#).

Mg# of Olivine and Pyroxene in Each Chondrule. For 10 Allende chondrules selected for coordinated petrology-isotope study, we estimated primary Mg# ($[\text{MgO}]/[\text{MgO} + \text{FeO}]$ molar percent) of olivine and pyroxene using EPMA major element analyses ([Dataset S6](#)). The Mg# of olivine and pyroxene reflect the oxidation state of iron (Fe/FeO) and total iron content during chondrule formation (17), which helps us to determine the environment experienced during chondrule formation, such as oxygen fugacity. FeO-poor olivine grains in Allende chondrules sometimes show FeO enrichment toward the grain boundary, which might be caused by Fe–Mg diffusion during the thermal metamorphism on the parent body. Therefore, for chondrules with high Mg# (> 95), we compared Mg# of multiple olivine and low-Ca pyroxene analyses from a single chondrule and applied either the maximum Fo contents of olivine or the maximum Mg# of low-Ca pyroxene, whichever was the highest, to be representative Mg# for the chondrule (13, 16).

Oxygen Isotope Mixing Model for Chondrules in a Dust-Enriched System. A study by ref. 17 constructed a mass balance model to relate O isotope ratios ($\Delta^{17}\text{O}$) and Mg# of CR chondrite chondrules that show negative correlation between $\Delta^{17}\text{O}$ and Mg# as a function of dust-enrichment factor and ratio of H_2O ice to anhydrous silicate dust. Here, the modified model by ref. 14 was used to explain $\Delta^{17}\text{O}$ versus Mg# relationship for chondrules in CV3 (Fig. 5). The model assumes that dust-enriched system consists of solar gas ($\Delta^{17}\text{O} = -28.4\%$), anhydrous silicate dust (-8.0%), organic matters ($+11.8\%$), and H_2O ice ($+2.0\%$). The model estimates oxygen fugacity relative to iron-wüstite (IW) buffer as a function of system atomic (H/O) and (C/O) ratios for given dust-enrichment factor relative to solar composition and H_2O ice enhancement relative to that of CI composition dust (17). The Mg# of mafic silicates are estimated as a function of oxygen fugacity. The $\Delta^{17}\text{O}$ value is estimated as mass balance of four components with distinct $\Delta^{17}\text{O}$ values. This model is not applicable to chondrules in ordinary chondrites that do not show a correlation between Mg# and $\Delta^{17}\text{O}$ (50). If ordinary chondrite-like chondrules formed under the presence of H_2O ice, flat $\Delta^{17}\text{O}$ values against Mg# indicate that H_2O ice had $\Delta^{17}\text{O}$ very similar to those of dust and the $\Delta^{17}\text{O}$ values would not be sensitive to abundance of H_2O ice in the chondrule precursors. For chondrules that formed under dry environments, dust-enrichment factors are estimated from chondrule Mg# using the case with $0 \times \text{CI}$ ice enhancement factor in the model. However, if chondrule precursors are depleted in total iron relative to CI abundance, the estimated dust-enrichment factors would be underestimated.

Ti-Cr-O Isotope Mixing Models. Two-component isotope mixing models in Figs. 3 and 4 were constructed using CAI and noncarbonaceous endmembers. CAIs were assumed to have $\epsilon^{50}\text{Ti}$, $\epsilon^{54}\text{Cr}$, and $\Delta^{17}\text{O}$ values of 9, 5, and -25 , respectively. The ratio of Ti, Cr, and O between CAI and noncarbonaceous endmembers was assumed to be ~ 10 , ~ 0.05 , and ~ 1 , respectively. These isotopic and elemental ratios were held constant and mixing lines were constructed to fit through (or close to) the individual chondrule data by adjusting the $\epsilon^{50}\text{Ti}$, $\epsilon^{54}\text{Cr}$, and $\Delta^{17}\text{O}$ values of the noncarbonaceous endmember. The $\epsilon^{50}\text{Ti}$ and $\epsilon^{54}\text{Cr}$ of AOAs was assumed to be similar to CAIs, for example forsterite-bearing CAIs (53). However, these curves are expected to be less hyperbolic than the CAI versus noncarbonaceous endmember mixing curves because the elemental ratios of Ti, Cr, and O between the AOAs and noncarbonaceous endmembers is less extreme (62).

Data Availability. All study data are included in the paper, [SI Appendix](#), and [Datasets S1–S6](#).

ACKNOWLEDGMENTS. We thank Nehru Cherukupalli (AMNH) for separating chondrules and Brian Hess for SIMS sample preparation. Additional chondrules were provided by the late Ian D. Hutcheon and the University of Alberta. The study was funded by NASA Emerging Worlds Grant NNX16AD34G awarded to Q.-Z.Y., NNX14AF29G to N.T.K. and NNX16AD37G to D.S.E. WiscSIMS is partly supported by NSF (EAR13-55590).

1. A. N. Krot, K. Keil, E. R. D. Scott, C. A. Goodrich, M. K. Weisberg, "Classification of meteorites" in *Treatise on Geochemistry*, A. M. Davis, Ed. (Elsevier, ed. 2, 2014), pp. 83–128.
2. A. Trinquier *et al.*, Origin of nucleosynthetic isotope heterogeneity in the solar protoplanetary disk. *Science* **324**, 374–376 (2009).
3. Q.-Z. Yin *et al.*, ^{53}Mn - ^{53}Cr systematics of Allende chondrules and $\epsilon^{54}\text{Cr}$ - $\Delta^{17}\text{O}$ correlations in bulk carbonaceous chondrites" in *Lunar Planetary Science Conference XL*, (2009).
4. L. Qin, C. M. O'D. Alexander, R. W. Carlson, M. F. Horan, T. Yokoyama, Contributors to chromium isotope variation of meteorites. *Geochim. Cosmochim. Acta* **74**, 1122–1145 (2010).
5. P. H. Warren, Stable-isotopic anomalies and the accretionary assemblage of the Earth and Mars: A subordinate role for carbonaceous chondrites. *Earth Planet. Sci. Lett.* **311**, 93–100 (2011).
6. K. D. McKeegan *et al.*, The oxygen isotopic composition of the Sun inferred from captured solar wind. *Science* **332**, 1528–1532 (2011).

7. T. S. Kruijjer, T. Kleine, L. E. Borg, The great isotopic dichotomy of the early Solar System. *Nat. Astron.* **4**, 32–40 (2020).
8. T. S. Kruijjer, C. Burkhardt, G. Budde, T. Kleine, Age of Jupiter inferred from the distinct genetics and formation times of meteorites. *Proc. Natl. Acad. Sci. U.S.A.* **114**, 6712–6716 (2017).
9. M. B. Olsen, D. Wielandt, M. Schiller, E. M. M. E. Van Kooten, M. Bizzarro, Magnesium and ⁵⁴Cr isotope compositions of carbonaceous chondrite chondrules - Insights into early disk processes. *Geochim. Cosmochim. Acta* **191**, 118–138 (2016).
10. E. M. M. E. Van Kooten et al., Isotopic evidence for primordial molecular cloud material in metal-rich carbonaceous chondrites. *Proc. Natl. Acad. Sci. U.S.A.* **113**, 2011–2016 (2016).
11. S. Gerber, C. Burkhardt, G. Budde, K. Metzler, T. Kleine, Mixing and Transport of Dust in the early solar nebula as inferred from titanium isotope variations among chondrules. *Astrophys. J.* **841**, L17 (2017).
12. S. Ebert et al., Ti isotopic evidence for a non-CAI refractory component in the inner Solar System. *Earth Planet. Sci. Lett.* **498**, 257–265 (2018).
13. T. J. Tenner, M. Kimura, N. T. Kita, Oxygen isotope characteristics of chondrules from the Yamato-82094 ungrouped carbonaceous chondrite: Further evidence for common O-isotope environments sampled among carbonaceous chondrites. *Meteorit. Planet. Sci.* **52**, 268–294 (2017).
14. A. T. Hertwig, C. Defouilloy, N. T. Kita, Formation of chondrules in a moderately high dust enriched disk: Evidence from oxygen isotopes of chondrules from the Kaba CV3 chondrite. *Geochim. Cosmochim. Acta* **224**, 116–131 (2018).
15. A. T. Hertwig, K. Makoto, T. Ushikubo, C. Defouilloy, N. T. Kita, The ²⁶Al-²⁶Mg systematics of FeO-rich chondrules from Acfer 094: Two chondrule generations distinct in age and oxygen isotope ratios. *Geochim. Cosmochim. Acta* **253**, 111–126 (2019).
16. A. T. Hertwig, M. Kimura, C. Defouilloy, N. T. Kita, Oxygen isotope systematics of chondrule olivine, pyroxene, and plagioclase in one of the most pristine CV_{3Red} chondrites (Northwest Africa 8613). *Meteorit. Planet. Sci.* **54**, 2666–2685 (2019).
17. T. J. Tenner, D. Nakashima, T. Ushikubo, N. T. Kita, M. Weisberg, Oxygen isotope ratios of FeO-poor chondrules in CR3 chondrites: Influences of dust enrichment and H₂O during chondrule formation. *Geochim. Cosmochim. Acta* **148**, 228–250 (2015).
18. R. N. Clayton, T. K. Mayeda, J. N. Goswami, E. J. Olsen, Oxygen isotope studies of ordinary chondrites. *Geochim. Cosmochim. Acta* **55**, 2317–2337 (1991).
19. M. E. Sanborn et al., Carbonaceous achondrites Northwest Africa 6704/6693: Milestones for early Solar System chronology and genealogy. *Geochim. Cosmochim. Acta* **245**, 577–596 (2019).
20. A. Trinquier, J. Birck, C.-J. Allègre, Widespread ⁵⁴Cr heterogeneity in the inner solar system. *Astron. J.* **655**, 1179–1185 (2007).
21. A. Trinquier, J.-L. Birck, C. J. Allègre, C. Göpel, D. Ulfbeck, ⁵³Mn-⁵³Cr systematics of the early Solar System revisited. *Geochim. Cosmochim. Acta* **72**, 5146–5163 (2008).
22. I. Leya, M. Schönabächler, U. Wiechert, U. Krähenbühl, A. N. Halliday, Titanium isotopes and the radial heterogeneity of the solar system. *Earth Planet. Sci. Lett.* **266**, 233–244 (2008).
23. C. A. Goodrich et al., Petrogenesis and provenance of ungrouped achondrite Northwest Africa 7325 from petrology, trace elements, oxygen, chromium and titanium isotopes, and mid-IR spectroscopy. *Geochim. Cosmochim. Acta* **203**, 381–403 (2017).
24. S. Li et al., Evidence for a multilayered internal structure of the chondritic acapulcoite-lodranite parent asteroid. *Geochim. Cosmochim. Acta* **242**, 82–101 (2018).
25. C. D. K. Herd et al., The Northwest Africa 8159 martian meteorite: Expanding the martian sample suite to the early Amazonian field. *Geochim. Cosmochim. Acta* **218**, 1–26 (2017).
26. T. E. Bunch, A. J. Irving, D. Rumble, III, R. L. Korotev, "Evidence for a carbonaceous chondrite parent body with near-TFL oxygen isotopes from unique metachondrite Northwest Africa 2788" in *American Geophysical Union Fall Meeting* (2006), pp. P51E–1246.
27. A. Ruzicka, J. N. Grossman, A. Bouvier, C. D. K. Herd, C. B. Agee, The meteoritical bulletin, No. 102. *Meteorit. Planet. Sci.* **50**, 1662 (2015).
28. H. C. Connolly Jr. et al., The meteoritical bulletin, No. 93, 2008 March. *Meteorit. Planet. Sci.* **43**, 571–632 (2008).
29. K. G. Gardner-Vandy et al., The Tafassasset primitive achondrite: Insights into initial stages of planetary differentiation. *Geochim. Cosmochim. Acta* **85**, 142–159 (2012).
30. A. J. Irving et al., Northwest Africa 6704: A unique cumulate permafic achondrite containing sodic feldspar, awaruite, and "fluid" inclusions, with an oxygen isotopic composition in the acapulcoites-lodranite field. *Meteorit. Planet. Sci.* **74**, 5231 (2011).
31. R. Clayton, T. Mayeda, Oxygen isotope studies of carbonaceous chondrites. *Geochim. Cosmochim. Acta* **63**, 2089–2104 (1999).
32. D. L. Schrader et al., The formation and alteration of the Renazzo-like carbonaceous chondrites I: Implications of bulk-oxygen isotopic composition. *Geochim. Cosmochim. Acta* **75**, 308–325 (2011).
33. S. S. Russell et al., The meteoritical bulletin, No. 89, 2005 September. *Meteorit. Planet. Sci.* **40**, A201–A263 (2005).
34. R. N. Clayton, T. K. Mayeda, Formation of ureilites by nebular processes. *Geochim. Cosmochim. Acta* **52**, 1313–1318 (1988).
35. R. N. Clayton, T. K. Mayeda, Oxygen isotope studies of achondrites. *Geochim. Cosmochim. Acta* **60**, 1999–2017 (1996).
36. A. Ruzicka, J. N. Grossman, L. Garvie, The meteoritical bulletin, No. 100, 2014 June. *Meteorit. Planet. Sci.* **49**, E1–E101 (2014).
37. C. B. Agee et al., Unique meteorite from early Amazonian Mars: Water-rich basaltic breccia Northwest Africa 7034. *Science* **339**, 780–785 (2013).
38. A. J. Irving, T. E. Bunch, D. Rumble III, T. E. Larson, Metachondrites: Recrystallized and/or residual mantle rocks from multiple, large chondritic parent bodies. *68th Annual Meteoritical Society Meeting*, 5218 (2005).
39. R. A. Ziegler et al., Petrology, geochemistry, and likely provenance of unique achondrite Graves Nunataks 06128. *Lunar Planetary Science Conference XXXIX*, 2456 (2008).
40. A. W. Tait, A. G. Tomkins, B. M. Godel, S. A. Wilson, P. Hasalova, Investigation of the H7 ordinary chondrite, Watson 012: Implications for recognition and classification of Type 7 meteorites. *Geochim. Cosmochim. Acta* **134**, 175–196 (2014).
41. A. J. Irving et al., "Collisional disruption of a layered, differentiated CR parent body containing metamorphic and igneous lithologies overlain by a chondritic veneer" in *Lunar Planetary Science Conference XLV*, (2014), p. 2465.
42. P. G. Brown et al., The fall, recovery, orbit, and composition of the Tagish Lake meteorite: A new type of carbonaceous chondrite. *Science* **290**, 320–325 (2000).
43. J. N. Grossman, A. J. Brearley, The onset of metamorphism in ordinary and carbonaceous chondrites. *Meteorit. Planet. Sci.* **40**, 87–122 (2005).
44. N. G. Rudraswami, T. Ushikubo, D. Nakashima, N. T. Kita, Oxygen isotope systematics of chondrules in the Allende CV3 chondrite: High precision ion microprobe studies. *Geochim. Cosmochim. Acta* **75**, 7596–7611 (2011).
45. R. N. Clayton et al., "Oxygen isotopic composition of chondrules in Allende and ordinary chondrites" in *Chondrules and Their Origins*, E. A. King, Ed. (Lunar and Planetary Institute, 1983), pp. 37–43.
46. Z. A. Torrano et al., Titanium isotope signatures of calcium-aluminum-rich inclusions from CV and CK chondrites: Implications for early Solar System reservoirs and mixing. *Geochim. Cosmochim. Acta* **263**, 13–30 (2019).
47. T. Ushikubo, M. Kimura, N. T. Kita, J. W. Valley, Primordial oxygen isotope reservoirs of the solar nebula recorded in chondrules in Acfer 094 carbonaceous chondrite. *Geochim. Cosmochim. Acta* **90**, 242–264 (2012).
48. A. E. Rubin, J. T. Wasson, R. N. Clayton, T. K. Mayeda, Oxygen isotopes in chondrules and coarse-grained chondrule rims from the Allende meteorite. *Earth Planet. Sci. Lett.* **96**, 247–255 (1990).
49. R. H. Jones et al., Oxygen isotope heterogeneity in chondrules from the Mokoia CV3 carbonaceous chondrite. *Geochim. Cosmochim. Acta* **68**, 3423–3438 (2004).
50. N. T. Kita et al., High precision SIMS oxygen three isotope study of chondrules in LL3 chondrites: Role of ambient gas during chondrule formation. *Geochim. Cosmochim. Acta* **74**, 6610–6635 (2010).
51. T. Ushikubo, T. J. Tenner, H. Hiyagon, N. T. Kita, A long duration of the ¹⁶O-rich reservoir in the solar nebula, as recorded in fine-grained refractory inclusions from the least metamorphosed carbonaceous chondrites. *Geochim. Cosmochim. Acta* **201**, 103–122 (2017).
52. R. N. Clayton, N. Onuma, L. Grossman, T. K. Mayeda, Distribution of the pre-solar component in Allende and other carbonaceous chondrites. *Earth Planet. Sci. Lett.* **34**, 209–224 (1977).
53. J. I. Simon et al., Calcium and titanium isotope fractionation in refractory inclusions: Tracers of condensation and inheritance in the early solar protoplanetary disk. *Earth Planet. Sci. Lett.* **472**, 277–288 (2017).
54. N. Dauphas et al., Neutron-rich chromium isotope anomalies in supernova nanoparticles. *Astrophys. J.* **720**, 1577–1591 (2010).
55. A. N. Krot, K. Keil, Anorthite-rich chondrules in CR and CH carbonaceous chondrites: Genetic link between Ca, Al-rich inclusions and ferromagnesian chondrules. *Meteorit. Planet. Sci.* **37**, 91–111 (2002).
56. A. N. Krot, I. D. Hutcheon, K. Keil, Anorthite-rich chondrules in the reduced CV chondrites: Evidence for complex formation history and genetic links between CAIs and ferromagnesian chondrules. *Meteorit. Planet. Sci.* **37**, 155–182 (2002).
57. A. N. Krot et al., Ca,Al-rich inclusions, amoeboid olivine aggregates, and Al-rich chondrules from the unique carbonaceous chondrite Acfer 094: I. Mineralogy and petrology. *Geochim. Cosmochim. Acta* **68**, 2167–2184 (2004).
58. S. Maruyama, H. Yurimoto, S. Sueno, Oxygen isotope evidence regarding the formation of spinel-bearing chondrules. *Earth Planet. Sci. Lett.* **169**, 165–171 (1999).
59. S. Maruyama, H. Yurimoto, Relationships among O, Mg isotopes and the petrography of two spinel-bearing chondrules. *Geochim. Cosmochim. Acta* **67**, 3943–3957 (2003).
60. G. Libourel, A. N. Krot, T. Laurent, Role of gas-melt interaction during chondrule formation. *Earth Planet. Sci. Lett.* **251**, 232–240 (2006).
61. G. Libourel, M. Portail, Chondrules as direct thermochemical sensors of solar protoplanetary disk gas. *Sci. Adv.* **4**, r3321 (2018).
62. M. Komatsu et al., Mineralogy and petrography of amoeboid olivine aggregates from the reduced CV3 chondrites Efremovka, Leoville and Vigarano: Products of nebular condensation, accretion and annealing. *Meteorit. Planet. Sci.* **36**, 629–641 (2001).
63. Y. Marrocchi et al., Formation of CV chondrules by recycling of amoeboid olivine aggregate-like precursors. *Geochim. Cosmochim. Acta* **247**, 121–141 (2019).
64. S. J. Desch, A. Kalyaan, C. M. O. Alexander, The effect of Jupiter's formation on the distribution of refractory elements and inclusions in meteorites. *Astrophys. J.* **238**, 11 (2018).
65. J. N. Cuzzi, S. S. Davis, A. R. Dobrovolskis, Blowing in the wind. II. Creation and redistribution of refractory inclusions in a turbulent protoplanetary nebula. *Icarus* **166**, 385–402 (2003).

66. F. J. Ciesla, Outward transport of high-temperature materials around the midplane of the solar nebula. *Science* **318**, 613–615 (2007).
67. F. J. Ciesla, The distributions and ages of refractory objects in the solar nebula. *Icarus* **208**, 455–467 (2010).
68. K. A. Kretke, D. N. C. Lin, Grain retention and formation of planetesimals near the Snow line in MRI-driven turbulent protoplanetary disks. *Astrophys. J.* **664**, L55–L58 (2007).
69. D. Bockelée-Morvan, D. Gautier, F. Hersant, J.-M. Huré, F. Robert, Turbulent radial mixing in the solar nebula as the source of crystalline silicates in comets. *Astron. Astrophys.* **384**, 1107–1118 (2002).
70. D. L. Schrader *et al.*, Distribution of ^{26}Al in the CR chondrite chondrule-forming region of the protoplanetary disk. *Geochim. Cosmochim. Acta* **201**, 275–302 (2017).
71. J. M. Friedrich *et al.*, Chondrule size and related physical properties: A compilation and evaluation of current data across all meteorite groups. *Chemie der Erde Geochim.* **75**, 419–443 (2015).
72. A. Yamakawa, K. Yamashita, A. Makishima, E. Nakamura, Chemical separation and mass spectrometry of Cr, Fe, Ni, Zn, and Cu in terrestrial and extraterrestrial materials using thermal ionization mass spectrometry. *Anal. Chem.* **81**, 9787–9794 (2009).
73. J. Zhang, N. Dauphas, A. M. Davis, A. Pourmand, A new method for MC-ICPMS measurement of titanium isotopic composition: Identification of correlated isotope anomalies in meteorites. *J. Anal. At. Spectrom.* **26**, 2197–2205 (2011).
74. W. R. Shields, T. J. Murphy, E. J. Catanzaro, E. L. Garner, Absolute isotopic abundance ratios and the atomic weight of a reference sample of chromium. *J. Res. Natl. Bur. Stand., A Phys. Chem.* **70A**, 193–197 (1966).
75. F. Niederer, D. Papanastassiou, G. Wasserburg, Absolute isotopic abundances of Ti in meteorites. *Geochim. Cosmochim. Acta* **49**, 835–851 (1985).
76. D. McDougal *et al.*, Intermineral oxygen three-isotope systematics of silicate minerals in equilibrated ordinary chondrites. *Meteorit. Planet. Sci.* **52**, 2322–2342 (2017).